PHYSICAL REVIEW E **108**, 054204 (2023)

Time-delay-induced spiral chimeras on a spherical surface of globally coupled oscillators

Ryong-Son Kim and Chol-Ung Choe *
Research Group for Nonlinear Dynamics, Department of Physics, University of Science, Unjong-District, Pyongyang, Democratic People's Republic of Korea

(Received 19 April 2023; accepted 13 October 2023; published 6 November 2023)

We consider globally coupled networks of identical oscillators, located on the surface of a sphere with interaction time delays, and show that the distance-dependent time delays play a key role for the spiral chimeras to occur as a generic state in different systems of coupled oscillators. For the phase oscillator system, we analyze the existence and stability of stationary solutions along the Ott-Antonsen invariant manifold to find the bifurcation structure of the spiral chimera state. We demonstrate via an extensive numerical experiment that the time-delay-induced spiral chimeras are also present for coupled networks of the Stuart-Landau and Van der Pol oscillators in the same parameter regime as that of phase oscillators, with a series of evenly spaced band-type regions. It is found that the spiral chimera state occurs as a consequence of a resonant-type interplay between the intrinsic period of an individual oscillator and the interaction time delay as a topological structure property.

DOI: 10.1103/PhysRevE.108.054204

I. INTRODUCTION

Collective behaviors in complex networks of coupled units have attracted great attention in recent years in the field of nonlinear science. In particular, the synchronization in systems of coupled oscillators provides a unifying framework in many contexts of physical, biological, and chemical systems [1–5]. The spiral wave is an important synchronous pattern appearing in continuous media, such as reaction-diffusion systems. The spiral waves are ubiquitous in chemical or biological systems [6], e.g., in cardiac muscle during the ventricular fibrillation [7–10] and in brain tissue [11].

One of the fascinating recent topics in the coupled oscillator system is the phenomenon of chimera states which are characterized by a hybrid nature of coexisting spatially coherent and incoherent domains [12,13]. As a symmetry-breaking phenomenon, the chimeras have attracted great interest and have been intensively studied, as illustrated in Refs. [14–19].

A particularly remarkable chimera state is the spiral chimera [20–22], which consists of a phase-randomized core of desynchronized oscillators surrounded by a spiral wave of synchronized oscillators. The spiral chimera states are known to occur mainly in discrete media, e.g., two-dimensional arrays of nonlocally coupled oscillators, and their properties differ from those of classical spiral wave patterns in continuous media. Such spiral chimeras were found in various topologies of networks, including a plane [21,23–25], a flat torus [26–30], and a spherical surface [30–36]. The spiral chimera state has been experimentally verified using the Belousov-Zhabotinsky chemical oscillator system [37,38]. Most of the spiral wave chimeras found so far have been in oscillator systems with nonlocal coupling, for which the coupling strength between oscillators varies with the distance between them.

Recently, we reported on spiral wave chimeras observed in the numerical simulations of globally coupled oscillators with heterogeneous time delays [36]. The heterogeneous delay times are ubiquitous in physical and biological systems, arising from finite propagation speeds of signals, finite chemical reaction times, and finite response times of synapses [39–43]. It is therefore important to identify the origin and nature of such a spiral chimera state caused by the heterogeneous interaction time delays. On the other hand, the spherical surface is topologically equivalent to the surfaces of different physical and biological systems, e.g., the human heart and brain, and the spiral chimeras on the sphere show an intriguing similarity to patterns of activity displayed by the human heart during ventricular fibrillation [10].

In this paper, we consider networks of all-to-all coupled oscillators located on the surface of a sphere with a simple distance-dependent interaction time delay. We investigate the existence and stability of different stationary states using analytical and numerical methods, which reveals that the time-delay induced spiral chimeras occur as a generic state in systems of the phase oscillators as well as the amplitude-phase oscillators. For the phase oscillator system, we analyze the existence and stability of different stationary states on the basis of Ott-Antonsen reduction theory [44,45] to find bifurcation structures of the spiral chimera patterns. In the coupled networks of the Stuart-Landau and Van der Pol oscillators, we provide an extensive numerical scan of the parameter variations and uncover the stability regions of spiral chimeras. We find that different networks of oscillators considered here exhibit striking similarities in the stability regions, with a series of the band-shaped parameter areas. This suggests that the stable spiral chimeras occur as a consequence of a resonant-type interplay between the intrinsic period of the respective local unit and the interaction time delay as a topological structure property.

*cholung-choe@star-co.net.kp

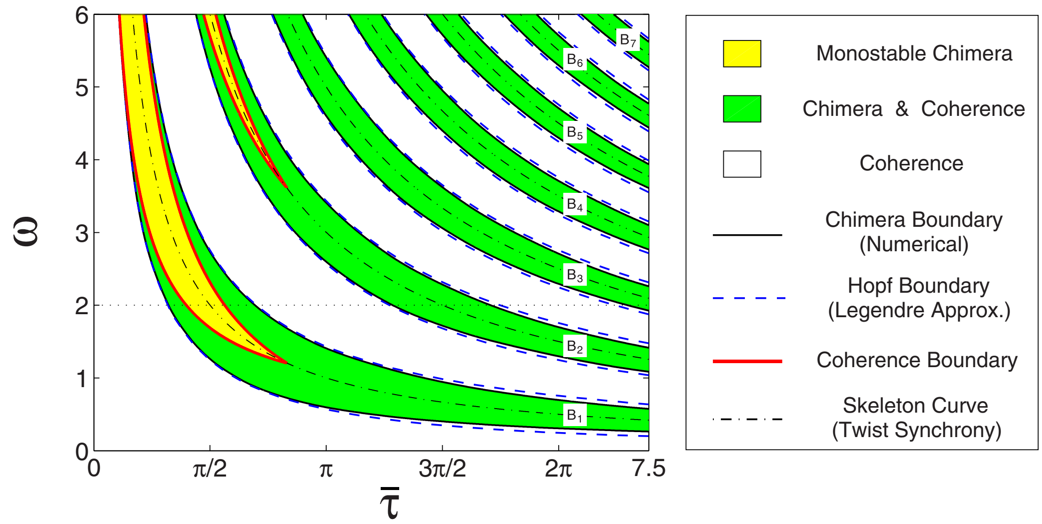

FIG. 1. Stability diagram of Eqs. (1) and (2) in the $(\bar{\tau}, \omega)$ plane for $\epsilon = 1$. Stable spiral chimeras occur in a series of band regions B_n enclosed by solid black line, determined by direct numerical simulations. Dashed blue lines denote theoretical prediction for Hopf boundaries of chimera bands, obtained by using the first-order Legendre series approximation. Green regions indicate multistable regime where the stable spiral chimera and coherent states coexist, while yellow regions correspond to monostable regime of spiral chimera. Red bold lines are stability boundaries of the coherent state, determined explicitly via Eq. (32). Dash-dotted lines denote the skeleton curves of chimera band B_n, given by $\omega\bar{\tau} = (2n-1)\pi$, where the twist-synchrony state appears. Dotted horizontal line marks the parameter interval, along which stability analyses are carried out in Figs. 2–4.

II. RESULTS

A. Governing equations

1. Model

We consider a two-dimensional large system of identical phase oscillators coupled with heterogeneous time delays, evolving according to

$$\frac{\partial \psi(\mathbf{r},t)}{\partial t} = \omega + \frac{\epsilon}{4\pi}\int_{\mathbb{S}^2} \sin[\psi(\mathbf{r}', t-\tau(\mathbf{r},\mathbf{r}')) - \psi(\mathbf{r},t)]d\mathbf{r}', \tag{1}$$

where $\psi(\mathbf{r},t)$ is the phase of the oscillator at position $\mathbf{r} \in \mathbb{S}^2$, ω is the natural frequency, ϵ characterizes the coupling strength, and $\mathbb{S}^2$ denotes the surface of the unit sphere. The function $\tau(\mathbf{r},\mathbf{r}')$ specifies the distance-dependent interaction time delays, arising from the finite speed of signal transmission between two positions $\mathbf{r}$ and $\mathbf{r}'$.

To ensure the symmetric coupling structure in Eq. (1), the delay function $\tau(\mathbf{r},\mathbf{r}')$ is assumed to depend only on the great circle distance between two points $\mathbf{r}$ and $\mathbf{r}'$ on the unit sphere $\mathbb{S}^2$, given by $\gamma(\mathbf{r},\mathbf{r}') = \arccos(\mathbf{r}\cdot\mathbf{r}')$. In this paper, we consider the simplest possible form of distance-dependent time delays given by a step function

$$\tau(\mathbf{r},\mathbf{r}') = \begin{cases} 0 & \text{if } 0 < \gamma(\mathbf{r},\mathbf{r}') \leqslant \frac{1}{2}\pi \\ \bar{\tau} & \text{if } \frac{1}{2}\pi < \gamma(\mathbf{r},\mathbf{r}') \leqslant \pi. \end{cases} \tag{2}$$

We note that, in contrast to the case without delays, the natural frequency ω cannot be eliminated from Eq. (1) by going to a rotating frame, $\psi \to \psi + \omega t$. In this paper, the frequency ω is considered as a main control parameter of the model system (1), along with time delay $\bar{\tau}$.

2. System reduction

To characterize spatial coherence and incoherence of chimera states, we define a complex order parameter $Z \equiv Re^{i\Psi}$ as

$$Z(\mathbf{r},t) = \frac{\epsilon}{4\pi}\int_{\mathbb{S}^2} \exp[i\psi(\mathbf{r}', t-\tau(\mathbf{r},\mathbf{r}'))]d\mathbf{r}'. \tag{3}$$

For a large system of phase oscillators, the macroscopic behavior can be represented by the probability density function $f(\psi,\mathbf{r},t)$, which reflects the probability that the oscillator at position $\mathbf{r}$ and at time t has the phase ψ.

By applying the Ott-Antonsen ansatz theory [44], we find that the evolution equation for $f(\psi,\mathbf{r},t)$ is reduced to a low-dimensional system for a complex-valued function $z(\mathbf{r},t)$ as following

$$\frac{\partial z(\mathbf{r},t)}{\partial t} = i\omega z + \frac{1}{2}(Z - z^2 Z^*), \tag{4a}$$

$$Z(\mathbf{r},t) = \frac{\epsilon}{4\pi}\int_{\mathbb{S}^2} z(\mathbf{r}', t-\tau(\mathbf{r},\mathbf{r}'))d\mathbf{r}', \tag{4b}$$

where the solutions satisfying $|z| \leqslant 1$ are only physically meaningful (for detailed derivation, see Appendix A).

B. Main results

In Fig. 1, the results from the numerical simulations of model system (1) and (2) and analytical investigations of the reduced system (4) are summarized, showing a stability diagram for the spiral chimera and coherent states in the $(\bar{\tau}, \omega)$ plane for $\epsilon = 1$.

Stable coherent state where all the oscillators are locked at the same phase appears in the white and green regions, which have been determined via the linear stability analysis of the reduced system (4), as shown in Sec. IV A. In the white

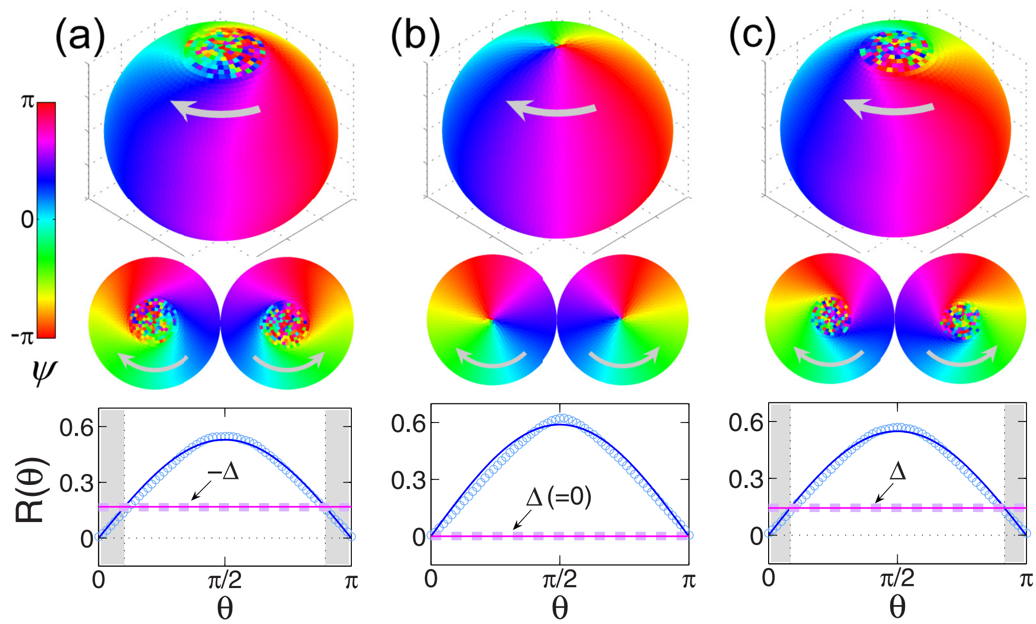

FIG. 2. Phase snapshot and longitudinal profile of spiral chimera states obtained by numerical simulations of Eqs. (1) and (2) with 5023 oscillators for $\epsilon = 1$, $\omega = 2$, and different values of time delay $\bar{\tau}$. (a) Spiral chimera state for $\bar{\tau} = \frac{\pi}{2} - 0.5$. Upper panel: Phase snapshot on sphere and its two-dimensional projections viewed from the north and south poles. Arrows indicate the rotation of spiral arms. Lower panel: Longitudinal profile of order parameter Z (open circles) and value of Δ (dashed bold line), calculated from spatiotemporal data of upper panel. Solid blue and magenta lines correspond to theoretical predictions for $R(\theta)$ and Δ, respectively, resulting from the first-order approximation given by Eq. (21). Gray boxes in the lower panels of Fig. 2 denote the incoherent domain. (b) Twist state with beach-ball pattern for $\bar{\tau} = \frac{\pi}{2}$. Spiral arms coincide with longitudinal lines, while incoherent-core region as well as value of Δ vanish. (c) Spiral chimera for $\bar{\tau} = \frac{\pi}{2} + 0.5$. Spiral arms are in reversed directions with respect to longitudinal lines and Δ takes opposite sign, as compared to those of (a).

regions, one or more stable coherent states with different collective frequencies could exist (see Sec. III B) but the spiral chimera state is unstable. While in the green region, one or more stable coherent states coexist with stable spiral chimeras. The stability boundaries for the coherent state, marked by red bold lines in Fig. 1, are explicitly given by Eq. (32).

The parameter regions for the stable spiral chimera state (yellow- and green-colored areas) have been obtained by direct numerical simulations of the discretized version of Eqs. (1) and (2),

$$\dot{\psi}_j = \omega + \frac{\epsilon}{N}\sum_{k=1}^{N}\sin[\psi_k(t - \tau(\mathbf{r}_j, \mathbf{r}_k)) - \psi_j], \qquad (5)$$

using the fourth-order Runge-Kutta method with a time step of 0.02s. To distribute an arbitrary number of points uniformly on the spherical surface, we take off the surface of a sphere in the form of a narrow spiral band that runs from the north pole to south pole, similar to paring an apple. Along the spiral band, we select the evenly spaced points at every interval equal to the width of the band, and then assign numbers to the points by one-dimensional index, $i = 1, 2, \ldots, N$. Given the number N, the spacing of points along the spiral equal to the width of the band is identified and one obtains nearly uniformly distributed points on $\mathbb{S}^2$ (see MATLAB codes for uniform distribution of points on the spheric surface in the Supplemental Material [46]). The slight nonuniformity in the density of points occurs mainly around two poles, which becomes weak as N increases.

Stable spiral chimeras were found to occur in a series of band regions B_n, enclosed by solid black lines. The dashed blue lines indicate the Hopf boundaries for the spiral chimeras, obtained by the first-order Legendre series approximation to the coupling kernel function, see Sec. IV C. This theoretical result shows good agreement with that of numerical simulations marked by solid lines. The green regions in Fig. 1 denote the bistable regime where either the coherent or spiral chimera states could occur, depending on the initial conditions: the former and latter ones are achieved when we start the system from a nearly in-phase state and a spiral wave with two phase defects, respectively. In the yellow regions, only the spiral chimera state occurs, independent of the initial conditions. The skeleton curves inside the chimera bands B_n, marked by dash-dotted lines, are given by Eq. (20), which correspond to the twist synchrony state with a beach-ball pattern, as illustrated in Fig. 2(b).

Figure 2 shows typical examples of spiral chimeras and twist-synchrony state, obtained by numerically integrating Eqs. (5). Figure 2(b) corresponds to the parameter values located on the skeleton curve of the chimera band B_1, which shows the twist-synchrony state with the beach-ball pattern. The parameter values of Figs. 2(a) and 2(c) lie, respectively, to the left and right of those of Fig. 2(b) on the horizontal parameter interval in Fig. 1, for which the spiral arms of synchronized oscillators are in opposite directions with respect to the meridian lines, as seen in the phase snapshots of the upper panels. One observes in Figs. 2(a) and 2(c) that the spiral arms near the drifting cores rotate inward and outward, respectively, and thus the corresponding chimera states can be considered to be antispiral and spiral chimeras [47,48]. The transition from spiral chimera to antispiral chimera occurs on the skeleton curves of chimera band B_n, given by $\omega\bar{\tau} = (2n-1)\pi$.

In the lower panels of Fig. 2, the longitudinal profiles $R(\theta)$ of order parameter and the corresponding phase velocity mismatch Δ, as defined in Eqs. (6), are displayed in the open circles and dashed lines, respectively. Numerically, the order parameter was quantified by Eq. (3), while the Δ value was evaluated by using the phase velocity of oscillators in the coherent domain. One can see that the values of Δ become negative, zero, and positive in Figs. 2(a)–2(c), respectively. The theoretical results from the first-order approximation to the order parameter Z, given by Eq. (21), are drawn with solid lines, which shows good agreement with the result from direct numerical simulations.

III. STATISTICALLY STATIONARY STATES

A. Self-consistency equation

Many dynamical regimes of interest occur as a stationary pattern in a rotating coordinate frame with a (yet unknown) collective frequency Ω. Applying the transformations $z \to ze^{i\Omega t}$ and $Z \to Ze^{i\Omega t}$, Eqs. (4) can be written by

$$\frac{\partial z(\mathbf{r},t)}{\partial t} = i\Delta z + \frac{1}{2}(Z - z^2 Z^*), \tag{6a}$$

$$Z(\mathbf{r},t) = \frac{\epsilon}{4\pi}\int_{\mathbb{S}^2} e^{-i\Omega\tau(\mathbf{r},\mathbf{r}')} z(\mathbf{r}', t-\tau(\mathbf{r},\mathbf{r}'))d\mathbf{r}', \tag{6b}$$

where $\Delta \equiv \omega - \Omega$.

The stationary spatial profiles of the rotating waves correspond to the fixed points of Eqs. (6):

$$z_0(\mathbf{r}) = ih(\mathbf{r})Z(\mathbf{r}), \tag{7}$$

where $h(\mathbf{r}) = \frac{1}{R^2(\mathbf{r})}(\Delta - \sqrt{\Delta^2 - R^2(\mathbf{r})})$ and $R(\mathbf{r}) \equiv |Z(\mathbf{r})|$. Inserting Eq. (7) into Eq. (6b), one obtains the self-consistency equation for the complex order parameter $Z(\mathbf{r})$ as

$$Z(\mathbf{r}) = \frac{i\epsilon}{4\pi}\int_{\mathbb{S}^2} G(\mathbf{r},\mathbf{r}')h(\mathbf{r}')Z(\mathbf{r}')d\mathbf{r}', \tag{8}$$

where the kernel $G(\mathbf{r},\mathbf{r}')$ is given by

$$G(\mathbf{r},\mathbf{r}') = \exp[-i\Omega\tau(\mathbf{r},\mathbf{r}')]. \tag{9}$$

We note that the function $h(\mathbf{r})$ depends on the absolute value of $Z(\mathbf{r})$ and thus Eq. (8) describes a nonlinear eigenvalue problem for the complex eigenfunction $Z(\mathbf{r})$ and the real eigenvalue Δ. If Z satisfies Eq. (8), so does $Ze^{i\Psi_0}$ for any constant angle Ψ_0. Thereby, we can arbitrarily specify the value of $\Psi(\mathbf{r})$ at any point $\mathbf{r}$ we like.

For the chimera states, the spatial regions satisfying $R(\mathbf{r}) \geqslant |\Delta|$ and $R(\mathbf{r}) < |\Delta|$ correspond to the coherent and incoherent domains, respectively.

B. Coherent state

For the spatially uniform state given by $Z = R = \text{const}$, Eq. (8) can be explicitly solved. Taking into account that $\frac{1}{4\pi}\int_{\mathbb{S}^2} e^{-i\Omega\tau(\mathbf{r},\mathbf{r}')}d\mathbf{r}' = \frac{1}{2}(1 + e^{-i\Omega\bar{\tau}})$, we separate the self-consistency Eq. (8) into the real and imaginary parts and find that the solutions for the coherent state are implicitly given by

$$\Omega = \omega - \frac{\epsilon}{2}\sin(\Omega\bar{\tau}), \tag{10a}$$

$$R = \epsilon|\cos(\Omega\bar{\tau}/2)|, \tag{10b}$$

$$z_0 = e^{i\Omega\bar{\tau}/2}. \tag{10c}$$

Figure 3(a) shows the solutions of Ω and $|Z|$ for the coherent state according to Eqs. (10a) and (10b) in dependence on the time delay $\bar{\tau}$ for parameter values $\epsilon = 1$ and $\omega = 2$. The collective frequency Ω is distributed around the intrinsic frequency ω, where multiple solutions are obtained with increasing time delay $\bar{\tau}$. The collective amplitude R also exhibits a multivalued behavior. The unstable branches of multivalued solutions are denoted as dashed curves. There is an interval of time delay $\bar{\tau}$, marked by shaded region, where no stable coherent states exist. Such a stability result follows from the eigenvalue analysis of the characteristic Eq. (31), shown in Fig. 3(b). This specifies the parameter region for the monostable spiral chimera state shown in Fig. 1.

C. Spiral chimera state

1. Expansion of coupling kernel

The distance-dependent kernel G given by Eq. (9) can be expanded via the Legendre polynomials of $\cos\gamma$ as

$$G(\mathbf{r},\mathbf{r}') = \sum_{\ell=0}^{\infty}\kappa_\ell P_\ell(\cos\gamma), \tag{11}$$

where P_ℓ is the Legendre polynomial of order ℓ and the coefficients κ_ℓ are given by $\kappa_\ell = \frac{2\ell+1}{2}\int_{-1}^{1} G(x)P_\ell(x)dx$. For the time-delay function $\tau(\mathbf{r},\mathbf{r}')$ given by Eq. (2), we obtain the expression for the coefficients κ_ℓ as follows:

$$\kappa_\ell = \begin{cases} \frac{1}{2}(1 + e^{-i\Omega\bar{\tau}}) & \text{for } \ell = 0 \\ 0 & \text{for even } \ell \\ \frac{1}{2}(2\ell+1)p_\ell(1 - e^{-i\Omega\bar{\tau}}) & \text{for odd } \ell, \end{cases} \tag{12}$$

where $p_\ell = \int_0^1 P_\ell(x)dx$, e.g., $p_1 = \frac{1}{2}$, $p_3 = \frac{-1}{8}$, $p_5 = \frac{1}{16}$, ...

Finding solutions of Eq. (8) for spatially inhomogeneous states is a difficult task, because the coupling kernel G is inseparable in $\mathbf{r}$ and $\mathbf{r}'$. To search for the chimera solutions approximately, we use a finite Lth-order approximation obtained from truncating the Legendre series (11) as follows:

$$G_L(\mathbf{r},\mathbf{r}') = \sum_{\ell=0}^{L}\kappa_\ell P_\ell(\cos\gamma). \tag{13}$$

The Legendre sum (13) can be described in the form of separable kernel by applying the spherical harmonic addition theorem $P_\ell(\cos\gamma) = \frac{4\pi}{2\ell+1}\sum_{m=-\ell}^{\ell} Y_\ell^m(\mathbf{r})[Y_\ell^m(\mathbf{r}')]^*$, where $Y_\ell^m(\mathbf{r})$ is the spherical harmonics of degree ℓ and order m, defined by $Y_\ell^m(\theta,\phi) = (-1)^m\sqrt{\frac{(2\ell+1)}{4\pi}\frac{(\ell-m)!}{(\ell+m)!}}P_\ell^m(\cos\theta)e^{im\phi}$, and P_ℓ^m denotes the associated Legendre polynomials with the azimuthal angle $\phi \in [0, 2\pi)$ and the polar angle $\theta \in [0, \pi]$ in spherical polar coordinates.

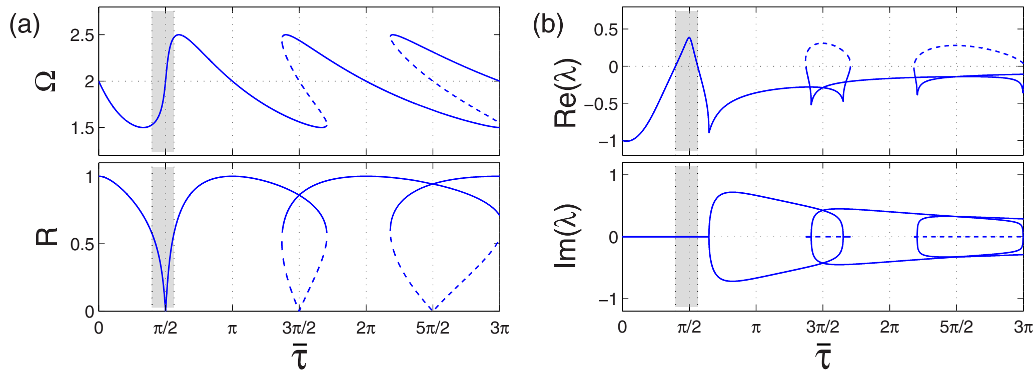

FIG. 3. Existence and stability of coherent states. (a) Collective frequency Ω and amplitude of Z for coherent states vs time delay $\bar{\tau}$, given by Eqs. (10). Dashed lines denote the unstable branches of multivalued solutions. (b) Real and imaginary parts of the rightmost eigenvalue for the coherent states vs time delay $\bar{\tau}$, determined by solving Eq. (31). Solid and dashed lines of both (a) and (b) correspond to each other. In the shaded region, no stable coherent states exist, which specify the monostable chimera region in Fig. 1. Parameters: $\epsilon = 1$ and $\omega = 2$, corresponding to the dotted horizontal line shown in Fig. 1.

2. Spiral chimera solutions

Substitution of Eqs. (13) into Eq. (8) and applying the spherical harmonic addition theorem yield a general expression of the order parameter as

$$Z(\mathbf{r}) = \sum_{\ell=0}^{L} \sum_{m=-\ell}^{\ell} c_{\ell m} Y_\ell^m(\mathbf{r}), \tag{14}$$

where the unknown coefficients are given by $c_{\ell m} = \frac{i\epsilon\kappa_\ell}{2\ell+1}\int_{\mathbb{S}^2} h(\mathbf{r}')[Y_\ell^m(\mathbf{r}')]^* Z(\mathbf{r}')d\mathbf{r}'$.

For the spiral wave ansatz given by

$$Z(\mathbf{r}) = \hat{Z}(\theta)e^{i\phi} \quad \text{with} \quad \hat{Z}(\theta) \equiv R(\theta)e^{i\Theta(\theta)}, \tag{15}$$

it holds that $c_{\ell m} = 0$ for all $m \neq 1$, and thus Eq. (14) is simplified to

$$Z_L(\mathbf{r}) = e^{i\phi}\sum_{\ell=1}^{L} a_\ell P_\ell^1(\cos\theta), \tag{16}$$

where

$$a_\ell = \frac{i\epsilon\kappa_\ell}{2\ell(\ell+1)}\int_0^\pi h(\theta')P_\ell^1(\cos\theta')\hat{Z}(\theta')\sin\theta' d\theta'. \tag{17}$$

Note that $a_\ell = 0$ for even ℓ since $\kappa_\ell = 0$.

Substituting Eq. (16) into Eq. (17), we obtain the reduced self-consistency equations for a_ℓ as follows:

$$a_\ell = \frac{i\epsilon\kappa_\ell}{\ell(\ell+1)}\sum_{n=1}^{L} a_n \langle h(x)P_\ell^1(x)P_n^1(x)\rangle, \tag{18}$$

where $h(x) = \frac{1}{\Delta + \sqrt{\Delta^2 - |\sum_{n=1}^{L} a_n P_n^1(x)|^2}}$ and the angular bracket denotes a spatial average defined by $\langle f\rangle \equiv \frac{1}{2}\int_{-1}^{1} f(x)dx$. The function $h(x)$ involves the L unknown quantities a_ℓ as well as a real Δ, and thus one has to solve L complex Eq. (18) for the $L+1$ unknowns $a_\ell \in \mathbb{C}$ and $\Delta \in \mathbb{R}$. By using the arbitrariness of choice of $\arg(Z) \equiv \Psi_0$, one of the L complex quantities a_ℓ can be set to be real, without loss of generality. This makes it possible to determine all the unknowns in terms of parameters $\bar{\tau}$, ω and ϵ in a closed form.

3. Twist-synchrony state

For the special case of $\Delta = 0$, Eq. (7) reduces to

$$z_0(\mathbf{r}) = e^{i[\phi+\Theta(\theta)]},$$

which represents a modulated coherent state. Furthermore, one can show that $\Theta(\theta) = 0$ for the spiral chimera ansatz (15). For proving this, we exploit the fact that for $\Delta = 0$, i.e. $\omega = \Omega$, Eq. (17) leads to

$$a_\ell = \frac{\epsilon\kappa_\ell}{2\ell(\ell+1)}\int_0^\pi P_\ell^1(\cos\theta')e^{i\Theta(\theta')}\sin\theta' d\theta',$$

where one of a_ℓ can be set to be purely real from the rotational invariance of $Z(\mathbf{r})$. This is possible only when the quantities $e^{i\Theta(\theta)}$ as well as κ_ℓ for odd ℓ, given by Eq. (12), become simultaneously real. Hence, it holds that $\Theta(\theta) = 0$ and $\omega\bar{\tau} = n\pi$ for $n \in \mathbb{Z}$. For κ_ℓ to be nonzero, the integers n should be odd. As a result, we find that the ϕ-twist synchrony state, given by

$$z_0(\mathbf{r}) = e^{i\phi} \quad \text{and} \quad Z(\mathbf{r}) = R(\theta)e^{i\phi}, \tag{19}$$

occurs for the parameter values that satisfy

$$\omega\bar{\tau} = (2n-1)\pi, \tag{20}$$

irrespective of the coupling strength ϵ. The twist synchrony state described by Eq. (19) shows a beach-ball pattern without incoherent domain. Such a beach-ball pattern is illustrated in Fig. 2(b), which corresponds to the parameter values $\omega = 2$ and $\bar{\tau} = \frac{\pi}{2}$ such that $\omega\bar{\tau} = \pi$.

Equation (20) for positive integers n specifies the skeleton curves of the chimera band B_n shown in Fig. 1. Note that the skeleton curve in the chimera band B_n is expressed by

$$\bar{\tau} = \tfrac{1}{2}(2n-1)T,$$

where $T \equiv \frac{2\pi}{\omega}$ denotes the intrinsic period of oscillator.

4. First-order approximation

We consider a particular example of the coupling kernel with $L = 1$, which has only two nonvanishing coefficients: $G_1(\mathbf{r}, \mathbf{r}') = \kappa_0 + \kappa_1\cos\gamma$. Then the order parameter (16) reduces to

$$Z_1 = a_1 \sin\theta e^{i\phi}, \tag{21}$$

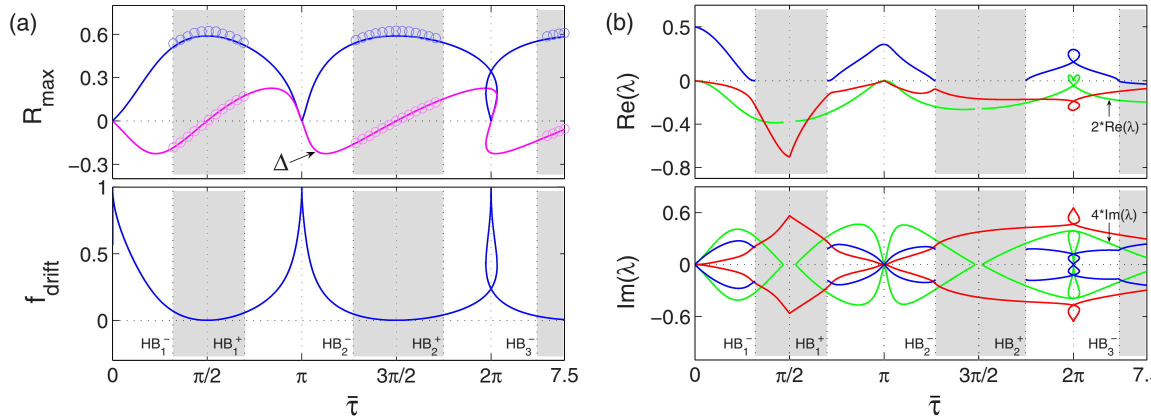

FIG. 4. Existence and stability of spiral chimera states. (a) Spiral chimera solutions to Eq. (23) vs time delay $\bar{\tau}$. Upper panel shows values of $\max R(\theta) \equiv a_1$ (blue line) and Δ (magenta line). The blue and magenta circles correspond to $|Z|_{\max}$ and Δ, respectively, determined by direct numerical simulations of Eqs. (1) and (2). Lower panel depicts the fraction of drifting oscillators, given by Eq. (24). (b) Real and imaginary parts of the rightmost point spectrums for chimera solutions of (a), determined by numerically solving Eq. (46). Shaded regions in both (a) and (b) indicate the stable regime of spiral chimeras. There occur Hopf-like bifurcations at the boundaries labeled $HB_n^{\pm}$ (see the text), which specify the Hopf boundaries, marked by dashed lines in Fig. 1. Parameters: Same as Fig. 3.

where a_1 can be assumed to be real by requiring $\arg(Z_1) = 0$ at the point $(\theta, \phi) = (\frac{\pi}{2}, 0)$. Then the self-consistency Eq. (18) is simplified to

$$2a_1^2 = i\epsilon\kappa_1\langle \Delta - \sqrt{\Delta^2 - a_1^2(1-x^2)}\rangle. \tag{22}$$

We note that the coefficient κ_1 is given by $\kappa_1 = \frac{3}{4}(1 - e^{-i\Omega\bar{\tau}})$, containing the unknown Ω. The integrations on the right-hand side of Eq. (22) can be calculated, which leads to

$$4a_1^2 = i\epsilon\kappa_1\left\{\Delta - \frac{a_1^2 - \Delta^2}{2a_1}\left(\ln\frac{a_1 - \Delta}{a_1 + \Delta} + i\pi\right)\right\}. \tag{23}$$

Two real unknowns a_1 and Δ (or equivalently Ω) for the chimera solution (21) are determined by solving Eq. (22) or, equivalently Eq. (23), in terms of parameters $\bar{\tau}$, ω, and ϵ. In the lower panels of Fig. 2, the solid lines indicate the longitudinal profile $R(\theta) \equiv a_1 \sin\theta$ and the corresponding value of Δ, determined by solving Eq. (23). One can see that for the first-order approximation, the theoretical result already exhibits good agreement with direct numerical simulations of the model system (1) and (2).

The coherence-incoherence boundary θ_c is determined by the intersection of two lines $R(\theta)$ and Δ (see Fig. 2, bottom panels), which yields $\theta_c = \arcsin\frac{|\Delta|}{a_1}$. Therefore, the fraction of drifting oscillators is given by

$$f_{\rm drift} = 1 - \sqrt{1 - \frac{\Delta^2}{a_1^2}}. \tag{24}$$

To search for the existence region of the spiral chimeras, we carried out numerical continuations of Eq. (22) by starting from the chimera states shown in Fig. 2 and varying the parameter values of $\bar{\tau}$, ω, and ϵ. The numerical continuations using the MATLAB root-finder "fsolve" reveal that the chimera solutions described by Eqs. (21) and (22) exist for the whole parameter region. Furthermore, due to the delayed coupling, multiple solutions with different amplitudes and locking frequencies become possible.

A typical result of numerically continuing the solutions as time delay $\bar{\tau}$ varies is shown in Fig. 4(a). The solutions to Eq. (22) and the fraction of drifting oscillators given by Eq. (24) are displayed with solid lines in the upper and lower panels, respectively. One can see that $a_1 = \frac{3\pi}{16}$ and $\Delta = f_{\rm drift} = 0$ when $\bar{\tau} = \frac{1}{2}(2n-1)\pi$, with $n \in \mathbb{Z}$, corresponding to parameter values located on the skeleton curve of chimera band B_n in Fig. 1. This leads to the twist-synchrony state with a beach-ball pattern, as shown in Fig. 2(b). When $\bar{\tau} = (n-1)\pi$ for $n \in \mathbb{Z}$, there exist solutions that satisfy $a_1 = \Delta = 0$ and $f_{\rm drift} = 1$, which correspond to the fully incoherent state. One observes multiple solutions near $\bar{\tau} = 2\pi$ and this behavior becomes more pronounced with increasing time delay $\bar{\tau}$.

Shaded regions of Fig. 4(a) indicate the stable parts of chimera solutions, which are identified by the stability analysis of the spiral chimeras [see Fig. 4(b)], studied in the next section. The open circles in Fig. 4(a) indicate the result from the direct numerical simulations of model systems (1) and (2), which are in good agreement with theoretical values represented by solid lines. One can observe that there are small discrepancies between the stability boundaries determined from the direct simulations and the first-order approximate scheme, which become more distinct for larger $\bar{\tau}$.

IV. STABILITY ANALYSIS

Substituting the ansatz $z(\mathbf{r}, t) = z_0(\mathbf{r}) + \xi(\mathbf{r}, t)$ with a small perturbation ξ into Eqs. (6) and linearizing the result with respect to ξ, we obtain the linear partial integrodifferential equation for $\xi \in \mathbb{C}$ as follows:

$$\frac{\partial\xi(\mathbf{r}, t)}{\partial t} = \eta(\mathbf{r})\xi + \frac{\epsilon}{2}\left(\mathcal{G}\xi - z_0^2(\mathbf{r})[\mathcal{G}\xi]^*\right), \tag{25}$$

where $\eta(\mathbf{r}) = i\Delta - z_0(\mathbf{r})Z^*(\mathbf{r})$ and $\mathcal{G}$ denotes a convolution operator defined by

$$(\mathcal{G}\xi)(\mathbf{r}, t) = \frac{1}{4\pi}\int_{\mathbb{S}^2} G(\mathbf{r}, \mathbf{r}')\xi(\mathbf{r}', t - \tau(\mathbf{r}, \mathbf{r}'))d\mathbf{r}'.$$

According to Eq. (7), we obtain

$$\eta(\mathbf{r}) = i\sqrt{\Delta^2 - R^2(\mathbf{r})}. \tag{26}$$

Note that Eq. (25) includes complex conjugated terms and hence cannot be treated as a regular complex equation. Instead, we consider an extended system by incorporating the complex conjugate counterpart of Eq. (25). These two equations form a closed system for the linear stability analysis, of which the right-hand side defines a linear operator $\mathcal{L}$,

$$\frac{\partial}{\partial t}\mathbf{p} = \mathcal{L}\mathbf{p}, \tag{27}$$

where $\mathbf{p} = (\xi, \xi^*)^T$.

Analytical treatment of time-delay equations like Eq. (27) is known to be difficult task in general. However, for the spatially uniform states, the stability analysis via Eq. (27) can be conducted rigorously, as shown in the next two subsections.

A. Stability of coherent state

We expand the perturbations ξ and ξ^* in terms of spherical harmonics as follows:

$$\xi(\mathbf{r}, t) = \sum_{k=0}^{\infty}\sum_{m=-k}^{k} a_{km}(t)Y_k^m(\mathbf{r}),$$

$$\xi^*(\mathbf{r}, t) = \sum_{k=0}^{\infty}\sum_{m=-k}^{k} b_{km}(t)Y_k^m(\mathbf{r}).$$

Applying the convolution operator gives

$$(\mathcal{G}\xi)(\mathbf{r}, t) = \sum_{k=0}^{\infty}\sum_{m=-k}^{k} a_{km}(t)\big\langle\Gamma^+(\mathbf{r}, \mathbf{r}')Y_k^m(\mathbf{r}')\big\rangle_{\mathbf{r}'},$$

$$(\mathcal{G}\xi)^*(\mathbf{r}, t) = \sum_{k=0}^{\infty}\sum_{m=-k}^{k} b_{km}(t)\big\langle\Gamma^-(\mathbf{r}, \mathbf{r}')Y_k^m(\mathbf{r}')\big\rangle_{\mathbf{r}'},$$

where

$$\Gamma^{\pm}(\mathbf{r}, \mathbf{r}') \equiv \exp\left[-(\lambda \pm i\Omega)\tau(\mathbf{r}, \mathbf{r}')\right]$$

and the angular bracket with index $\mathbf{r}'$ represents a spatial average over the surface of the sphere: $\langle f(\mathbf{r}, \mathbf{r}')\rangle_{\mathbf{r}'} \equiv \frac{1}{4\pi}\int_{\mathbb{S}^2} f(\mathbf{r}, \mathbf{r}')d\mathbf{r}' = \frac{1}{4\pi}\int_0^{\pi}\sin\theta\int_0^{2\pi} f(\theta, \phi; \theta', \phi')d\phi' d\theta'$.

Expanding the kernels $\Gamma^{\pm}$ via the Legendre polynomials, one obtains

$$\Gamma^{\pm}(\mathbf{r}, \mathbf{r}') = \sum_{k=0}^{\infty}\chi_\ell^{\pm}P_\ell(\cos\gamma), \tag{28}$$

where the coefficients are given by

$$\chi_\ell^{\pm}(\lambda) = \begin{cases} \frac{1}{2}[1 + e^{-(\lambda \pm i\Omega)\bar{\tau}}] & \text{for } \ell = 0 \\ 0 & \text{for even } \ell \\ \frac{1}{2}p_\ell(2\ell+1)[1 - e^{-(\lambda \pm i\Omega)\bar{\tau}}] & \text{for odd } \ell. \end{cases} \tag{29}$$

Applying the spherical harmonic addition theorem gives the convolution expressions as $(\mathcal{G}\xi)(\mathbf{r}, t) = \sum_{\ell=0}^{\infty}\sum_{m=-\ell}^{\ell}\frac{\chi_\ell^+(\lambda)}{2\ell+1}a_{\ell m}(t)Y_\ell^m(\mathbf{r})$ and $(\mathcal{G}\xi)^*(\mathbf{r}, t) = \sum_{\ell=0}^{\infty}\sum_{m=-\ell}^{\ell}\frac{\chi_\ell^-(\lambda)}{2\ell+1}b_{\ell m}(t)Y_\ell^m(\mathbf{r})$. Hence, for the spatially uniform functions η and z_0, Eq. (27) reduces to

$$\begin{pmatrix}\dot{a}_{\ell m} \\ \dot{b}_{\ell m}\end{pmatrix} = \begin{pmatrix}\eta + \frac{\epsilon\chi_\ell^+}{2(2\ell+1)} & \frac{-\epsilon z_0^2\chi_\ell^-}{2(2\ell+1)} \\ \frac{-\epsilon z_0^{*2}\chi_\ell^+}{2(2\ell+1)} & \eta + \frac{\epsilon\chi_\ell^-}{2(2\ell+1)}\end{pmatrix}\begin{pmatrix}a_{\ell m} \\ b_{\ell m}\end{pmatrix}.$$

Letting $a_{\ell m}(t) = \hat{a}_{\ell m}e^{\lambda t}$ and $b_{\ell m}(t) = \hat{b}_{\ell m}e^{\lambda t}$, we find implicitly the eigenvalues for the coherent state as

$$\lambda^{(1)} = \eta \quad \text{and} \quad \lambda_\ell^{(2)} = \eta + \frac{\epsilon[\chi_\ell^+(\lambda) + \chi_\ell^-(\lambda)]}{2(2\ell+1)}. \tag{30}$$

Taking into account that $\chi_\ell = 0$ for even ℓ and $\eta = \frac{-\epsilon}{2}(1 + \cos\Omega\bar{\tau})$, one obtains nonpositive eigenvalues for even ℓ:

$$\lambda^{(1)} = \lambda_\ell^{(2)} = -\frac{\epsilon}{2}(1 + \cos\Omega\bar{\tau}) \leqslant 0.$$

Equation (30) for $\ell = 0$ reads

$$\lambda = \frac{\epsilon}{2}(e^{-\lambda\bar{\tau}} - 1)\cos\Omega\bar{\tau},$$

for which $\lambda = 0$ obviously becomes a solution. This zero eigenvalue reflects that perturbations along a direction tangent to the synchronization manifold neither grow nor decay.

The eigenvalues for odd ℓ satisfy the equation

$$\lambda = \frac{\epsilon}{2}[p_\ell - 1 - (p_\ell e^{-\lambda\bar{\tau}} + 1)\cos\Omega\bar{\tau}]. \tag{31}$$

The coherent state becomes stable when the real parts of eigenvalues that obey Eq. (31) are all negative.

Figure 3(b) depicts the dependence of the real and imaginary parts of the leading eigenvalue λ upon the time delay $\bar{\tau}$ according to Eq. (31) for $\ell = 1$, where the Ω values determined in Fig. 3(a) are used. The shaded region indicates the interval of $\bar{\tau}$ where no stable coherent states exist. Both end points of the $\bar{\tau}$ interval determine the stability boundaries for the monostable chimera state, as shown with red bold lines in Fig. 1. A pair of stability boundaries for the monostable chimera, existing inside the chimera band B_n, can be determined by putting $\lambda = 0$ and $\ell = 1$ in Eq. (31), which results in

$$\bar{\tau}_+ = \frac{1}{\Omega_+}\left[2(n-1)\pi + \arccos\frac{p_1 - 1}{p_1 + 1}\right], \tag{32a}$$

$$\bar{\tau}_- = \frac{1}{\Omega_-}\left[2n\pi - \arccos\frac{p_1 - 1}{p_1 + 1}\right], \tag{32b}$$

where $p_1 = 1/2$ and the subindices $+$ and $-$ denote the upper and lower boundaries, respectively. According to Eq. (10a), Ω_+ and Ω_- are given by $\Omega_{\pm} = \omega \mp \frac{\epsilon\sqrt{p_1}}{p_1+1}$. The intersection of two boundaries occurs when $\bar{\tau}_+$ equals $\bar{\tau}_-$, and thus the crossing point $(\bar{\tau}_c, \omega_c)$ is determined as $\bar{\tau}_c = \frac{p_1+1}{\epsilon\sqrt{p_1}}[\pi - \arccos\frac{p_1-1}{p_1+1}]$ and $\omega_c = \frac{\sqrt{p_1}}{p_1+1}\frac{(2n-1)\pi\epsilon}{\pi - \arccos\frac{p_1-1}{p_1+1}}$. One can see immediately that

$$\omega_c\bar{\tau}_c = (2n-1)\pi,$$

irrespective of parameter ϵ. Taking into account Eq. (20), this implies that the intersection point of the stability boundaries for the monostable chimeras lies on the skeleton curve of the chimera band B_n, which is clearly visible in Fig. 1.

B. Stability of incoherent states

We recall that the trivial solution $z(\mathbf{r}, t) = 0$ of Eqs. (4) denotes the completely incoherent state, for which the perturbative equation becomes simply

$$\frac{\partial \xi(\mathbf{r}, t)}{\partial t} = i\omega\xi(\mathbf{r}, t) + \frac{\epsilon}{2}\hat{\mathcal{G}}\xi, \tag{33}$$

where $\hat{\mathcal{G}}\xi = \frac{1}{4\pi}\int_{\mathbb{S}^2} \hat{G}(\mathbf{r}, \mathbf{r}')\xi(\mathbf{r}', t)d\mathbf{r}'$ and $\hat{G}(\mathbf{r}, \mathbf{r}') \equiv \exp(-\lambda\tau(\mathbf{r}, \mathbf{r}'))$. We expand the perturbation ξ and convolution $\hat{\mathcal{G}}\xi$ in terms of spherical harmonics as $\xi(\mathbf{r}, t) = \sum_{\ell=0}^{\infty}\sum_{m=-\ell}^{\ell} \hat{a}_{\ell m}(t)Y_\ell^m(\mathbf{r})$ and $\hat{\mathcal{G}}\xi = \sum_{\ell=0}^{\infty}\sum_{m=-\ell}^{\ell} \hat{a}_{\ell m}(t)\langle\hat{G}(\mathbf{r}, \mathbf{r}')Y_\ell^m(\mathbf{r}')\rangle_{\mathbf{r}'}$.

Expanding kernel $\hat{G}$ via the Legendre series as $\hat{G}(\mathbf{r}, \mathbf{r}') = \sum_{k=0}^{\infty} \hat{\chi}_\ell P_\ell(\cos\gamma)$ and applying the spherical harmonic addition theorem into Eq. (33), one obtains

$$\dot{\hat{a}}_{\ell m} = i\omega\hat{a}_{\ell m} + \tfrac{\epsilon\hat{\chi}_\ell(\lambda)}{2(2\ell+1)}\hat{a}_{\ell m},$$

where

$$\hat{\chi}_\ell(\lambda) = \begin{cases} \frac{1}{2}(1 + e^{-\lambda\bar{\tau}}) & \text{for } \ell = 0 \\ 0 & \text{for even } \ell \\ \frac{1}{2}p_\ell(2\ell + 1)(1 - e^{-\lambda\bar{\tau}}) & \text{for odd } \ell. \end{cases}$$

Using the ansatz $\hat{a}_{\ell m}(t) = \bar{a}_{\ell m}e^{\lambda t}$, we find the characteristic equations for the incoherent state as follows:

$$\lambda = i\omega + \frac{\epsilon\hat{\chi}_\ell(\lambda)}{2(2\ell + 1)}, \tag{34}$$

which yields $\lambda = i\omega$ for even ℓ and $\lambda = i\omega + \frac{\epsilon}{4}p_\ell(1 - e^{-\lambda\bar{\tau}})$ for odd ℓ. The leading eigenvalues are determined by Eq. (34) for $\ell = 0$, which reads

$$\lambda = i\omega + \frac{\epsilon}{4}(1 + e^{-\lambda\bar{\tau}}). \tag{35}$$

One can prove that all roots of Eq. (35) lie in the right half-plane $\mathrm{Re}(\lambda) > 0$ for any $\epsilon > 0$. The eigenvalue λ depends continuously on the time delay $\bar{\tau}$. For zero delay, it is obvious that $\mathrm{Re}(\lambda) > 0$. For the change of stability to occur, we need the eigenvalues to cross into the left half-plane through the imaginary axis as $\bar{\tau}$ varies, and the critical values of $\bar{\tau}$ must correspond to a pure imaginary eigenvalue $\lambda = i\sigma$ with $\sigma \in \mathbb{R}$. Since Eq. (35) does not allow for such solutions, we can conclude that all the eigenvalues stay in the right half-plane forever, which implies that the incoherent state never becomes stable.

C. Stability of spiral chimera state

For the finite-order approximation to the coupling kernel G, the perturbative equation (25) can be written by

$$\frac{\partial \xi(\mathbf{r}, t)}{\partial t} = \eta(\mathbf{r})\xi + \frac{\epsilon}{2}\left(\mathcal{G}_L\xi - z_0^2(\mathbf{r})[\mathcal{G}_L\xi]^*\right), \tag{36}$$

where the convolution operator $\mathcal{G}_L$ is defined by

$$(\mathcal{G}_L\xi)(\mathbf{r}, t) = \frac{1}{4\pi}\int_{\mathbb{S}^2} G_L(\mathbf{r}, \mathbf{r}')\xi(\mathbf{r}', t - \tau(\mathbf{r}, \mathbf{r}'))d\mathbf{r}',$$

with the kernel function G_L given by Eq. (13). Since Eq. (36) includes only separable kernels, the linear stability analysis for the spiral chimera states, which was described in Secs. III C 2–III C 4, can be performed.

We substitute the ansatz in the form of

$$\begin{pmatrix}\xi \\ \xi^*\end{pmatrix} = \begin{pmatrix}q_1(\mathbf{r}) \\ q_2(\mathbf{r})\end{pmatrix}e^{\lambda t}$$

into the perturbative system consisting of Eq. (36) and its complex conjugate to obtain

$$\lambda q_1 = \eta q_1 + \tfrac{\epsilon}{2}\langle\Gamma_L^+(\mathbf{r}, \mathbf{r}')q_1(\mathbf{r}') - [z_0(\mathbf{r})]^2\Gamma_L^-(\mathbf{r}, \mathbf{r}')q_2(\mathbf{r}')\rangle_{\mathbf{r}'},$$
$$\lambda q_2 = \eta^* q_2 + \tfrac{\epsilon}{2}\langle\Gamma_L^-(\mathbf{r}, \mathbf{r}')q_2(\mathbf{r}') - [z_0^*(\mathbf{r})]^2\Gamma_L^+(\mathbf{r}, \mathbf{r}')q_1(\mathbf{r}')\rangle_{\mathbf{r}'},$$

where $\Gamma_L^\pm$ denotes the Lth-rank approximation of $\Gamma^\pm$ given by Eq. (28): $\Gamma_L^\pm(\mathbf{r}, \mathbf{r}') = \sum_{\ell=0}^{L}\chi_\ell^\pm(\lambda)P_\ell(\cos\gamma)$. Applying the spherical harmonic addition theorem and integrating with respect to $\mathbf{r}'$ leads to

$$\lambda\mathbf{q}(\mathbf{r}) = J(\mathbf{r})\mathbf{q}(\mathbf{r}) + \sum_{\ell=0}^{L}\sum_{m=-\ell}^{\ell} Y_\ell^m(\mathbf{r})Q_\ell(\mathbf{r}; \lambda)\mathbf{c}_{\ell m}, \tag{37}$$

where $\mathbf{q}(\mathbf{r}) = \begin{pmatrix}q_1(\mathbf{r}) \\ q_2(\mathbf{r})\end{pmatrix}$, $J(\mathbf{r}) = \begin{pmatrix}\eta(\mathbf{r}) & 0 \\ 0 & \eta^*(\mathbf{r})\end{pmatrix}$,

$$Q_\ell(\mathbf{r}; \lambda) = \frac{2\pi\epsilon}{2\ell + 1}\begin{pmatrix}\chi_\ell^+(\lambda) & -z_0^2(\mathbf{r})\chi_\ell^-(\lambda) \\ -z_0^{*2}(\mathbf{r})\chi_\ell^+(\lambda) & \chi_\ell^-(\lambda)\end{pmatrix}, \tag{38}$$

and the constant vectors $\mathbf{c}_{\ell m}$ are given by

$$\mathbf{c}_{\ell m} = \left\langle\left[Y_\ell^m(\mathbf{r}')\right]^*\mathbf{q}(\mathbf{r}')\right\rangle_{\mathbf{r}'}. \tag{39}$$

1. Point spectrum

Now we assume that $\det[\lambda I_2 - J(\mathbf{r})] \neq 0$, where I_2 denotes the 2×2 identity matrix. Solving Eq. (37) for $\mathbf{q}(\mathbf{r})$ and substituting it into Eq. (39), we obtain homogeneous equations for the $(L + 1)^2$ constant vectors $\mathbf{c}_{\ell m}$ as follows:

$$\mathbf{c}_{\ell m} = \sum_{k=1}^{L}\sum_{n=-k}^{k}\left\langle\left[Y_\ell^m(\mathbf{r})\right]^*Y_k^n(\mathbf{r})E(\mathbf{r}; \lambda)Q_k(\mathbf{r}; \lambda)\right\rangle_{\mathbf{r}}\mathbf{c}_{kn}, \tag{40}$$

where

$$E(\mathbf{r}; \lambda) = [\lambda I_2 - J(\mathbf{r})]^{-1}. \tag{41}$$

Renumbering the $(L + 1)^2$ functions Y_ℓ^m and $\mathbf{c}_{\ell m}$ so $(Y_1, Y_2, \ldots, Y_{(L+1)^2})^T := (Y_0^0, Y_1^{-1}, Y_1^0, Y_1^1, \ldots, Y_L^{-L}, Y_L^{-L+1}, \ldots, Y_L^L)^T$ and $(\mathbf{c}_1, \mathbf{c}_2, \ldots, \mathbf{c}_{(L+1)^2})^T := (\mathbf{c}_{00}, \mathbf{c}_{1,-1}, \mathbf{c}_{10}, \mathbf{c}_{11}, \ldots, \mathbf{c}_{L,-L}, \mathbf{c}_{L,-L+1}, \ldots, \mathbf{c}_{LL})^T$, and also introducing the $(L + 1)^2$ functions $\bar{Q}_j$ such that $(\bar{Q}_1, \bar{Q}_2, \ldots, \bar{Q}_{(L+1)^2})^T := (Q_0, Q_1, Q_1, Q_1, Q_2, \ldots, Q_L)^T$, then Eq. (40) can be rewritten in the form of

$$\mathbf{c}_j = \sum_{k=1}^{(L+1)^2} B_{jk}(\lambda)\mathbf{c}_k, \quad j = 1, \ldots, (L + 1)^2,$$

where B_{jk} is a two-dimensional matrix given by

$$B_{jk}(\lambda) = \langle Y_j^*(\mathbf{r})Y_k(\mathbf{r})E(\mathbf{r}; \lambda)\bar{Q}_k(\mathbf{r}; \lambda)\rangle_{\mathbf{r}}.$$

As a result, we obtain the characteristic equation for the *point* spectra λ of the Lth-order approximate chimera solutions as follows:

$$\det[B(\lambda) - \mathbf{I}] = 0, \tag{42}$$

where B denotes the matrix defined by $\{B_{jk}\}$ and $\mathbf{I}$ is the $2(L + 1)^2$-dimensional identity matrix.

2. Continuous spectrum

Another part of spectra of the operator $\mathcal{L}$ satisfies $\det[\lambda I_2 - J(\mathbf{r})] = 0$, which gives continuous spectra

$$\lambda = \eta(\mathbf{r}) \quad \text{and} \quad \lambda = \eta^*(\mathbf{r}).$$

Taking into account Eq. (26), one obtains the continuous spectrum for the coherent domain as

$$\lambda_{\text{coh}} = -\sqrt{R^2(\mathbf{r}) - \Delta^2} \tag{43}$$

and for the incoherent domain as

$$\lambda_{\text{incoh}} = \pm i\sqrt{\Delta^2 - R^2(\mathbf{r})}. \tag{44}$$

Thus, the spiral wave chimera state has a T-shaped continuous spectrum that consists of two intervals along the negative real and pure imaginary axes, which correspond to the coherent and incoherent domains, respectively.

3. First-order stability analysis

In the first-order approximation to the kernel function, given by G_1, the matrix $B(\lambda)$ consists of 4×4 matrix blocks as follows:

$$B(\lambda) = \begin{pmatrix} B_{11}(\lambda) & B_{12}(\lambda) & B_{13}(\lambda) & B_{14}(\lambda) \\ B_{21}(\lambda) & B_{22}(\lambda) & B_{23}(\lambda) & B_{24}(\lambda) \\ B_{31}(\lambda) & B_{32}(\lambda) & B_{33}(\lambda) & B_{34}(\lambda) \\ B_{41}(\lambda) & B_{42}(\lambda) & B_{43}(\lambda) & B_{44}(\lambda) \end{pmatrix}, \tag{45}$$

where $B_{11} = \langle |Y_0^0|^2 E Q_0\rangle_{\mathbf{r}}$, $B_{12} = \langle Y_0^0 Y_1^{-1} E Q_1\rangle_{\mathbf{r}}$, $B_{13} = \langle Y_0^0 Y_1^0 E Q_1\rangle_{\mathbf{r}}$, $B_{14} = \langle Y_0^0 Y_1^1 E Q_1\rangle_{\mathbf{r}}$, $B_{21} = \langle Y_1^{-1*} Y_0^0 E Q_0\rangle_{\mathbf{r}}$, $B_{22} = \langle |Y_1^{-1}|^2 E Q_1\rangle_{\mathbf{r}}$, $B_{23} = \langle Y_1^{-1*} Y_1^0 E Q_1\rangle_{\mathbf{r}}$, $B_{24} = \langle Y_1^{-1*} Y_1^1 E Q_1\rangle_{\mathbf{r}}$, $B_{31} = \langle Y_1^{0*} Y_0^0 E Q_0\rangle_{\mathbf{r}}$, $B_{32} = \langle Y_1^{0*} Y_1^{-1} E Q_1\rangle_{\mathbf{r}}$, $B_{33} = \langle |Y_1^0|^2 E Q_1\rangle_{\mathbf{r}}$, $B_{34} = \langle Y_1^{0*} Y_1^1 E Q_1\rangle_{\mathbf{r}}$, $B_{41} = \langle Y_1^{1*} Y_0^0 E Q_0\rangle_{\mathbf{r}}$, $B_{42} = \langle Y_1^{1*} Y_1^{-1} E Q_1\rangle_{\mathbf{r}}$, $B_{43} = \langle Y_1^{1*} Y_1^0 E Q_1\rangle_{\mathbf{r}}$, and $B_{44} = \langle |Y_1^1|^2 E Q_1\rangle_{\mathbf{r}}$.

Employing the symmetries of the spiral chimera solution given by Eq. (21), one can find that all the elements of matrix (45) are zero except for the following six blocks: B_{24}, B_{42}, and B_{jj} for $j = 1, \ldots, 4$ (see Appendix B). Thus the characteristic Eq. (42) factorizes into two subsystems as follows:

$$0 = \det[B_{11}(\lambda) - I_2], \tag{46a}$$

$$0 = \det\left[\begin{pmatrix} B_{22}(\lambda) & 0 & B_{24}(\lambda) \\ 0 & B_{33}(\lambda) & 0 \\ B_{42}(\lambda) & 0 & B_{44}(\lambda) \end{pmatrix} - I_6\right]. \tag{46b}$$

Each matrix block in Eq. (46) includes double integrals. For the spiral chimera represented by Eq. (21), the integrals with respect to the azimuthal angle $\phi \in [0, 2\pi)$ can be calculated, reducing the double integral calculations into a simple integration with respect to the polar angle θ, as outlined in Appendix B. This allows us to increase the speed and accuracy of all numerical calculations of the characteristic Eq. (46).

Solving numerically Eq. (46) for the spiral chimera state given by Eq. (21), we determined the point spectra. Figure 4(b) shows a typical result of numerically continuing the solutions of characteristic Eq. (46) as the time delay $\bar{\tau}$ varies. The parameters correspond to the parameter interval marked with the dotted horizontal line in Fig. 1. Three branches of the rightmost point spectra are sorted out with different colors.

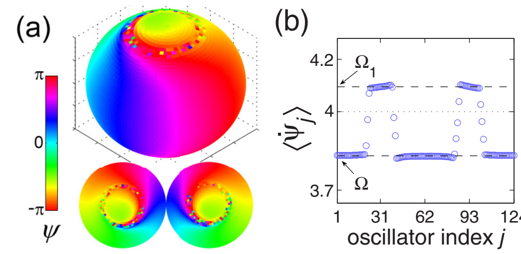

FIG. 5. (a) Phase snapshot of quasiperiodic (breathing) spiral chimera, obtained by integrating Eqs. (1) and (2) with 5023 oscillators for $\epsilon = 1$, $\omega = 4$, and $\bar{\tau} = 1.1$. (b) Mean phase velocities of 124 oscillators, located on a longitudinal thin slice of the spherical surface (see the text).

The blue and red lines are determined by Eq. (46a), while the green lines correspond to the result from Eq. (46b). One can observe that the point spectra, represented by blue and green lines, could emerge from and be absorbed into the T-shaped continuous spectra described by Eqs. (43) and (44) when $\bar{\tau}$ varies. Such behavior is known to be typical of the chimera states [34–36].

We see the $\bar{\tau}$ intervals with shaded backgrounds, for which the real parts of λ are all negative so the spiral chimera state becomes stable. With increasing $\bar{\tau}$, a pair of complex conjugate eigenvalues, denoted by blue lines, emerges suddenly from the imaginary axis of complex λ plane at the boundaries $HB_{1,2}^+$ and they move further into the right-half plane, destabilizing the chimera state. When a pair of unstable complex conjugate eigenvalues protrudes from the neutrally stable T-shaped continuous spectra, we call the bifurcation scenario the Hopf-like bifurcation. When passing through the boundaries $HB_{1,2}^-$, the chimera state becomes stable via an inverse Hopf-like bifurcation. The boundaries $HB_n^{\pm}$ of such Hopf-like bifurcations provide theoretical prediction for the stability boundaries of spiral chimera states and specify the Hopf boundaries, marked by dashed lines in Fig. 1.

The stability analysis using the first-order approximation suggests that the spiral chimera state actually undergoes destabilization via the Hopf-like bifurcation when passing beyond the boundaries of the chimera bands B_n.

4. Breathing spiral chimera state

Through the numerical simulations of Eqs. (1) and (2) for parameter values close to the stability boundaries of the chimera bands, we observed breathing spiral chimeras that exhibit a quasiperiodic behavior. Figure 5(a) depicts an example of the breathing spiral chimera state observed for the parameter values of $\epsilon = 1$, $\omega = 4$, and $\bar{\tau} = 1.1$. Such a breathing spiral chimera state is characterized by the appearance of a secondary coherent domain around the north and south poles. The incoherent oscillators are located in a narrow annular band outside the secondary coherence domains, as shown in Fig. 5(a).

Figure 5(b) displays averaged phase velocities, $\langle\dot{\psi}_j\rangle$, of oscillators located on a longitudinal slice of the spherical surface. The index j of oscillators on a longitudinal slice is chosen to start from an equatorial point and return back via the north pole, opposite the equatorial point, and south

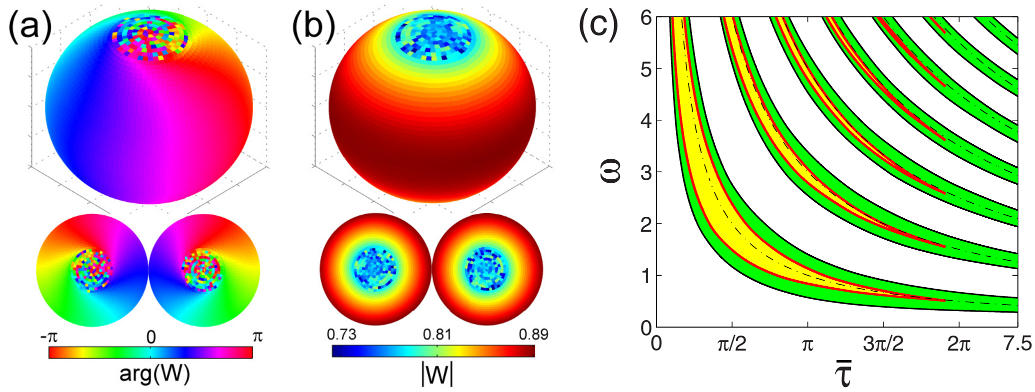

FIG. 6. Spiral chimera states in Stuart-Landau oscillators coupled with heterogeneous delays. [(a), (b)] Snapshots of the phase and amplitude of W_j, obtained by numerical integration of Eqs. (47) and (48) for $N = 5023$, $\sigma = 0.4$, $\omega = 2$, and $\bar{\tau} = 2.1$. (c) Stability diagram in the $(\bar{\tau}, \omega)$ plane for $\sigma = 0.4$, drawn in the same format as Fig. 1. All the stability boundaries are determined via extensive numerical simulations of Eqs. (47) and (48). Dash-dotted lines denote the skeleton curves of chimera band B_n, given by $\omega = (2n-1)\pi/\bar{\tau}$.

pole. Thus the oscillators for $j = 31$, 62 and 93 are located near north pole, equatorial point and south pole, respectively. The phase velocities were averaged over 200 units of time after cutting off the transients of $t = 200$. In Fig. 5(b), one can see that the oscillators located on the secondary coherent domain changes with a new frequency Ω_1 that differs from the collective frequency Ω of the primary coherent domain.

V. AMPLITUDE-PHASE OSCILLATORS WITH HETEROGENEOUS DELAY COUPLING

So far, we analyzed the chimeric behaviors in the system of coupled phase oscillators on the basis of the Ott-Antonsen reduction method. To examine whether the spiral chimera states could occur in networks of oscillators described by more than one variable, we now consider the amplitude-phase oscillator systems in which the reduction to phase oscillators cannot be performed.

A. Delay coupled Stuart-Landau oscillators

As a local system, we choose the Stuart-Landau oscillator described by a complex variables, which includes not only the phase but also amplitude dynamics. It is known that, in the system of Stuart-Landau oscillators with time-delay coupling, different behaviors from that seen in networks of phase oscillators, such as the amplitude death [49], could occur.

Consider a globally coupled network of N delay-coupled Stuart-Landau oscillators located on the surface of the unit sphere, whose dynamics is described by

$$\dot{W}_j = (1+i\omega-|W_j|^2)W_j + \frac{\sigma}{N}\sum_{n=1}^{N}[W_n(t-\tau_{jn}) - W_j(t)], \quad (47)$$

with $W_j \in \mathbb{C}$ for $j = 1, \dots, N$. Here ω is the natural frequency, $\sigma \in \mathbb{R}$ is the coupling strength, and τ_{jn} denotes the interaction time delays. The time delays τ_{jn} are assumed to depend on the distance γ_{jn} between two oscillators j and n on the unit sphere, given by $\gamma_{jn} = \arccos(\mathbf{r}_j \cdot \mathbf{r}_n)$. Like in Eq. (2), we choose a simple form of a distance-dependent time delay function given by

$$\tau_{jn} = \begin{cases} 0 & \text{if } 0 < \gamma_{jn} \leqslant \frac{1}{2}\pi \\ \bar{\tau} & \text{if } \frac{1}{2}\pi < \gamma_{jn} \leqslant \pi. \end{cases} \quad (48)$$

Our numerical simulations of Eqs. (47) and (48) reveal that the spiral chimeras induced by distance-dependent delays appear as a generic state in the Stuart-Landau system as well.

A representative spiral chimera state is depicted in Fig. 6. One can see that Stuart-Landau oscillators coupled with distance-dependent delays show chimeric behavior for *both* phases and amplitudes. In analogy with the pure phase oscillators system, the phases of complex variables W_j display the spiral wave chimera pattern, as seen in Fig. 6(a). While a spot-type chimera pattern is observed in the snapshot of amplitudes of W_j, as shown in Fig. 6(b), where the coherent and incoherent domains are clearly distinguished.

We explored extensively the parameter regions for the different types of the stationary states through numerical simulations of Eqs. (47) and (48). Figure 6(c) shows the stability regimes for the spiral chimera and coherent states in the $(\bar{\tau}, \omega)$ plane, whose format is the same as in Fig. 1. All the stability boundaries were determined by numerically continuing the integrations of Eqs. (47) and (48) with 5023 oscillators. One can see that there exist parameter regions for the spiral chimera state coexisting with coherent state (green region) as well as for those emerging as a unique attractor (yellow region). The incoherent state as well as the amplitude death were not observed in our numerical experiments, which implies they are unstable.

Remarkably, we see in Fig. 6(c) a complete resemblance in the shape of stability regions for the spiral chimera and coherent states, as compared to Fig. 1. The spiral chimeras occur in a series of band-shaped regions and, furthermore, their skeleton curves marked by dash-dotted lines obey exactly the same form as Eq. (20), i.e.,

$$\omega\bar{\tau} = (2n-1)\pi.$$

This implies that the spiral chimeras occur dominantly when the interaction time delay $\bar{\tau}$ is near to a half the odd number

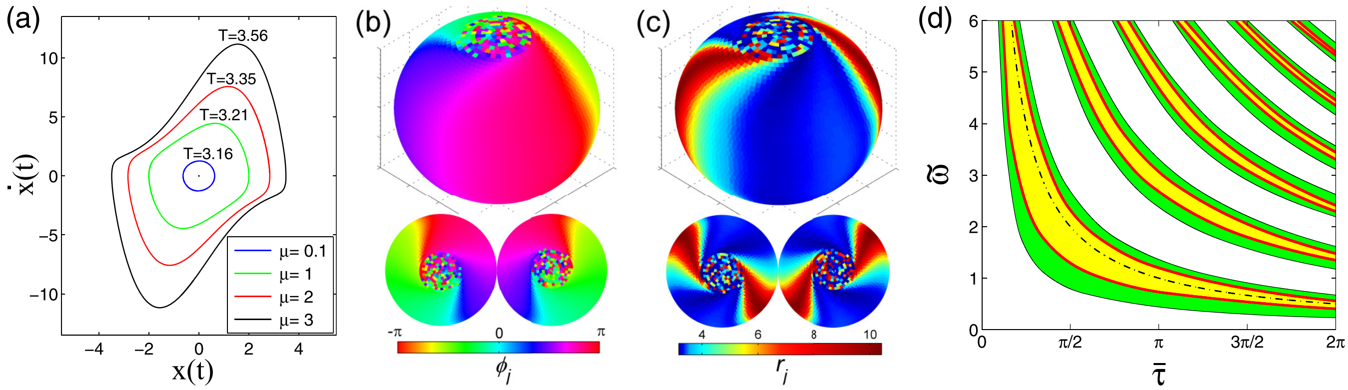

FIG. 7. Spiral chimera states in delay-coupled Van der Pol oscillators. (a) Limit cycles of a single Van der Pol oscillator for $\omega = 2$ and different values of μ. [(b), (c)] Snapshots of the geometric phases ϕ_j and amplitudes r_j, obtained by numerical integration of Eqs. (49) and (48) for $N = 5023$, $K = 0.5$, $\mu = 3$, $\omega = 2$, and $\bar{\tau} = 2$. (d) Stability diagram in the $(\bar{\tau}, \tilde{\omega})$ plane for $\mu = 3$ and $K = 0.5$, where $\tilde{\omega} \equiv 2\pi/T(\mu, \omega)$ denotes the intrinsic frequency of uncoupled relaxation oscillator. All the stability regions are determined via numerical simulations, drawn in the same format as Figs. 1 and 6(c). Dash-dotted line inside the primary chimera band is given by $\tilde{\omega} = \pi/\bar{\tau}$.

times the intrinsic period $T \equiv \frac{2\pi}{\omega}$ of decoupled oscillators as

$$\bar{\tau} \approx \left(n - \frac{1}{2}\right)T.$$

We note that the parameter regions of coherent states are distributed around the time delay values near to the integer times of the intrinsic period of oscillators:

$$\bar{\tau} \approx nT.$$

B. Delay-coupled Van der Pol oscillators

To show the universal occurrence of spiral wave chimeras owing to heterogeneous time delays, we now consider a system of N identical delay-coupled Van der Pol oscillators $x_j \in \mathbb{R}$, given by

$$\ddot{x}_j - (\mu - x_j^2)\dot{x}_j + \omega^2 x_j = \frac{K}{N}\sum_{n=1}^{N}[\dot{x}_n(t - \tau_{jn}) - \dot{x}_j]. \quad (49)$$

Here the parameter $\mu > 0$ determines the rate of attraction to the limit cycle of an individual oscillator with the natural frequency ω. The oscillators are arranged on the unit sphere with all-to-all coupling strength K and distance-dependent time delays τ_{jn} given by Eq. (48).

For sufficiently small μ, each uncoupled oscillator exhibits a periodic orbit on a circular limit cycle, whose period given by $T = T(\mu, \omega)$ reduces approximately to $T_0 \equiv \frac{2\pi}{\omega}$. While, for large μ, the limit cycle is not a circle and the waveform exhibits a strong nonlinear relaxation oscillation. Moreover, the dependence of intrinsic period T on parameter μ becomes pronounced. In Fig. 7(a), the intrinsic periods and shapes of the limit cycles of a decoupled Van der Pol oscillator are depicted for different values of μ. Larger values of μ result in an increasing amplitude of the limit cycle as well as an increasing period T. Below we deliberately choose the case of relaxation-type oscillations and fix the parameter μ at $\mu = 3$.

Our extensive numerical simulations of Eq. (49) with interaction time delays τ_{jn} given by Eq. (48) reveal that the spiral chimeras occur in a wide region of parameter space. Figures 7(b) and 7(c) illustrate the representative snapshots of the geometric phase ϕ_j and amplitude r_j, respectively, defined by

$$r_j(t)e^{i\phi_j(t)} \equiv x_j(t) + i\dot{x}_j(t).$$

Similar to the Stuart-Landau oscillator system, the Van der Pol oscillators coupled with distance-dependent delays provide chimeric behaviors in both the phases and amplitudes. The main difference is that, as shown in Figs. 7(c), the rotating spiral arms are observed in the coherent domain of amplitudes r_j as well.

Figure 7(d) summarizes the results obtained from the numerical simulations of Eq. (49), which shows the stability diagram in the $(\bar{\tau}, \tilde{\omega})$ plane with the intrinsic frequency $\tilde{\omega}$ of uncoupled relaxation oscillator, given by $\tilde{\omega} \equiv 2\pi/T(\mu, \omega)$. One observes again a close resemblance in the shape of stability regions with a series of evenly spaced chimera bands, as compared to Figs. 1 and 6. The parameter regions for the monostable spiral chimera states, denoted by yellow-colored area, are considerably enlarged for the delay-coupled Van der Pol oscillator system, in comparison with systems of phase oscillators and Stuart-Landau oscillators.

Furthermore, we see that the dash-dotted line, determined by $\tilde{\omega}\bar{\tau} = \pi$, might serve as a skeleton of the primary chimera band. This strongly suggests that it is universal for networks of oscillators with sinusoidal as well as nonsinusoidal limit cycles that the spiral chimeras appear to be stable, primarily for the interaction time delay near to half the period of individual oscillators, i.e., $\bar{\tau} \approx \frac{1}{2}T$. Meanwhile, the coherent state becomes stable near the time delays given by $\bar{\tau} = nT$ for integers n. These could be explained within the framework of the delayed feedback control (DFC) [50] to stabilize unstable periodic orbits (UPOs). The DFC uses the difference of the current and the delayed state, where the time delay τ is chosen to be the period T of the UPO, $\tau = T$. The DFC scheme applies to a single oscillator [51] as well as networks of coupled oscillators [52], where the latter case corresponds to the emergence of a coherent state of stabilized UPOs. For the case of $\tau \neq T$, e.g., $\tau \approx \frac{1}{2}T$, the DFC does not work and leads to desynchronization of UPOs, which could be interpreted as a counterpart of the spiral chimera state occurring close to $\bar{\tau} = \frac{1}{2}T$.

VI. CONCLUSIONS AND OUTLOOK

In this paper, we considered globally coupled networks of identical oscillators, distributed on a sphere with interaction time delay. It is demonstrated that in different systems of coupled oscillators, the distance-dependent time delay plays a key role for the spiral chimeras to occur as a generic state. We found that the spiral chimeras occur as a consequence of a resonant-type interplay between the intrinsic period of local unit and the interaction time delay as a topological structure property.

For the phase oscillator system, we have explored rigorous analyses for the existence and stability of different stationary states along the Ott-Antonsen invariant manifold to find the parameter regions of stable spiral chimera patterns. It has been found that the spiral chimeras occur stably in a series of the band-shaped parameter regions B_n, for which the skeleton curves obey an explicit relation between the intrinsic period T of uncoupled oscillator and the interaction time delay $\bar{\tau}$, as $\bar{\tau} = \frac{1}{2}(2n-1)T$, irrespective of the coupling strength ϵ. We determined analytically the stability regions where the spiral chimeras appear as a self-emerging state, irrespective of initial conditions.

We have provided an extensive numerical experiment for the delay-coupled networks of Stuart-Landau and Van der Pol oscillators, which reveals that the spiral chimera states in the phase-amplitude oscillator systems occur in very similar parameter regions to those of phase oscillator systems. In particular, the spiral chimera states appear to be stable when there is a strong correlation between the intrinsic period T of individual oscillator and the interaction time delay $\bar{\tau}$, regardless of the unit of network exhibiting oscillations on a sinusoidal or nonsinusoidal (relaxation-type) limit cycle. For example, the stable spiral chimera states, appearing inside the primary chimera band B_1, correspond to the resonance condition $\bar{\tau} = \frac{1}{2}T$.

In this paper, we chose the stepwise delay form (2) as a distance-dependent delay function, the main virtues of which were two: to diminish the massive computations in direct numerical simulations of model systems, owing to the otherwise overmany delay times, and to make the analytical description of spiral chimera states possible. However, in realistic systems such as laser networks or neural tissue, the interaction time delays appear to be proportional to the distance between two oscillators,

$$\tau(\mathbf{r}, \mathbf{r}') = \frac{\gamma(\mathbf{r}, \mathbf{r}')}{v}, \qquad (50)$$

where v is the signal propagation speed. Through the direct numerical simulations of Eqs. (1) and (50), we verified the stable spiral chimera states in wide parameter regions, as shown in Fig. 8(a). In contrast to the case of the stepwise time delays (2), for the interaction-delay function given by Eq. (50), there occurs not only the two-core spiral chimera but also higher-order spiral chimeras such as the four- and eight-core spiral

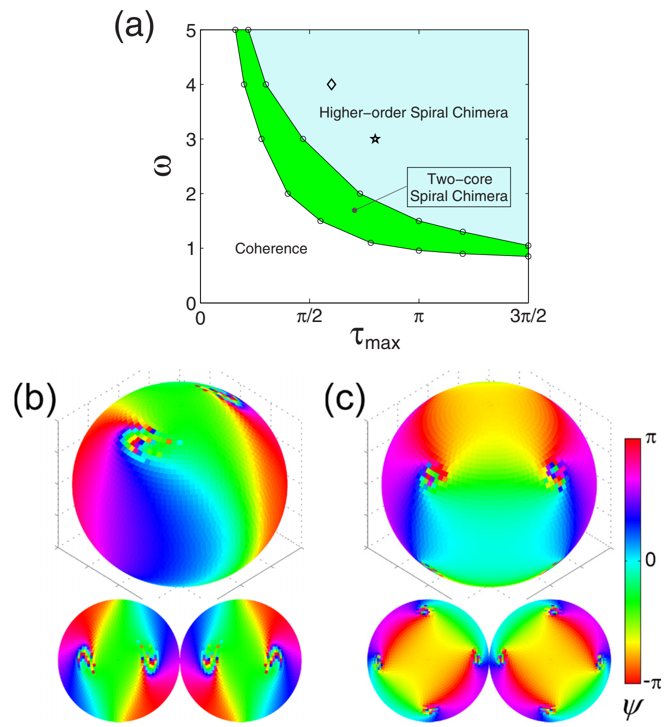

FIG. 8. Spiral chimeras for the distance-dependent delay function (50). (a) Stability diagram in the $(\tau_{\max}, \omega)$ plane with $\tau_{\max} \equiv \pi/v$, obtained by numerical integrations of Eqs. (1) and (50) for $N = 5023$ and $\epsilon = 1$. (b) Phase snapshot of four-core spiral chimera for $\tau_{\max} = 0.6\pi$ and $\omega = 4$, corresponding to the diamond displayed in (a). (c) Eight-core spiral chimera for $\tau_{\max} = 0.8\pi$ and $\omega = 3$, corresponding to the asterisk in (a).

chimeras, which are illustrated in Figs. 8(b) and 8(c), respectively. Furthermore, the two-core spiral chimera state occurs in the band-shaped green region in the $(\tau_{\max}, \omega)$ parameter plane, where $\tau_{\max} \equiv \frac{\pi}{v}$, which bears striking resemblance to the primary chimera band B_1 shown in Fig. 1. We can thus conclude that the distance-dependent time delays provide an essential and universal driving mechanism for the emergence of spiral chimera states.

The distance-dependent interaction time delays are omnipresent in nature and engineering systems, like semiconductor laser networks and neuroscience. We conjecture that the time-delay induced spiral chimeras could occur in many realistic systems of oscillators coupled with distance-dependent time delays. In particular, the resonance structure between the intrinsic period of local unit and the interaction time delay for the stable spiral chimera states might provide an important insight into the mechanisms that underlie the activity patterns displayed by the human heart during ventricular fibrillation.

APPENDIX A: DERIVATION OF REDUCED SYSTEM

By using the order parameter defined by Eq. (3), the model Eq. (1) can be rewritten in a decoupled form as follows:

$$\frac{\partial \psi(\mathbf{r}, t)}{\partial t} = \omega + \mathrm{Im}\big[Z(\mathbf{r}, t)e^{-i\psi(\mathbf{r}, t)}\big]. \qquad (A1)$$

The large system of the phase oscillators can be treated by the probability density function $f(\psi, \mathbf{r}, t)$, which satisfies the continuity equation

$$\frac{\partial f}{\partial t} + \frac{\partial}{\partial \psi}(fv) = 0, \tag{A2}$$

where $v = v(\psi, \mathbf{r}, t)$ is given, using Eq. (A1), as

$$v = \omega + \frac{\epsilon}{4\pi}\mathrm{Im}\left[e^{-i\psi}\int_{\mathbb{S}^2}\int_0^{2\pi} f(\psi', \mathbf{r}', t-\tau_{\mathbf{r},\mathbf{r}'})e^{i\psi'}d\psi' d\mathbf{r}'\right]. \tag{A3}$$

Following the Ott-Antonsen ansatz theory [44,45], we expand $f(\psi, \mathbf{r}, t)$ in a Fourier series with respect to ψ and restrict our analysis to a particular low-dimensional manifold defined by $c_n = c^n$, where c_n is the nth Fourier coefficient. Thus, we write

$$f(\psi, \mathbf{r}, t) = \frac{1}{2\pi}\left\{1 + \sum_{n=1}^{\infty}([z^*(\mathbf{r}, t)e^{i\psi}]^n + \text{c.c.})\right\}, \tag{A4}$$

where the asterisk denotes complex conjugate and c.c. stands for the complex conjugate of the preceding term.

Substituting Eqs. (A3) and (A4) into (A2), we obtain the Ott-Antonsen ansatz equation for the complex variable $z(\mathbf{r}, t)$ in the form of Eqs. (4). To avoid a divergence of the series (A4), it should be assumed that $|z(\mathbf{r}, t)| \leqslant 1$.

APPENDIX B: REDUCTION OF DOUBLE INTEGRALS IN MATRIX $B(\lambda)$

Multiplying the matrices (38) and (41) leads to

$$EQ_\ell = \frac{2\pi\epsilon}{2\ell+1}\begin{pmatrix} \frac{\chi_\ell^+(\lambda)}{\lambda-\eta} & \frac{-z_0^2\chi_\ell^-(\lambda)}{\lambda-\eta} \\ \frac{-z_0^{*2}\chi_\ell^+(\lambda)}{\lambda-\eta^*} & \frac{\chi_\ell^-(\lambda)}{\lambda-\eta^*} \end{pmatrix}.$$

For the spiral chimera states determined by Eqs. (21) and (22), the functions η and z_0 are given by

$$\eta(\theta) = i\sqrt{\Delta^2 - a_1^2\sin^2\theta},$$
$$z_0(\theta, \phi) = ih(\theta)a\sin\theta e^{i\phi}.$$

Then, the elements of matrix EQ_ℓ could only depend on the azimuthal angle ϕ as a function of $e^{2i\phi}$, which yields integral equalities $\int_0^{2\pi} EQ_\ell e^{\pm i\phi}d\phi = 0$. Thus the following eight matrix blocks in the matrix (45) vanish:

$$B_{12} = \frac{1}{4\pi}\sqrt{\frac{3}{2}}\langle EQ_1 \sin\theta e^{-i\phi}\rangle_{\mathbf{r}} = 0,$$
$$B_{14} = \frac{-1}{4\pi}\sqrt{\frac{3}{2}}\langle EQ_1 \sin\theta e^{i\phi}\rangle_{\mathbf{r}} = 0,$$
$$B_{21} = \frac{1}{4\pi}\sqrt{\frac{3}{2}}\langle EQ_0 \sin\theta e^{i\phi}\rangle_{\mathbf{r}} = 0,$$
$$B_{23} = \frac{3}{4\pi}\sqrt{\frac{1}{2}}\langle EQ_1 \sin\theta\cos\theta e^{i\phi}\rangle_{\mathbf{r}} = 0,$$
$$B_{32} = \frac{3}{4\pi}\sqrt{\frac{1}{2}}\langle EQ_1 \sin\theta\cos\theta e^{-i\phi}\rangle_{\mathbf{r}} = 0,$$
$$B_{34} = \frac{-3}{4\pi}\sqrt{\frac{1}{2}}\langle EQ_1 \sin\theta\cos\theta e^{i\phi}\rangle_{\mathbf{r}} = 0,$$
$$B_{41} = \frac{-1}{4\pi}\sqrt{\frac{3}{2}}\langle EQ_0 \sin\theta e^{-i\phi}\rangle_{\mathbf{r}} = 0,$$
$$B_{43} = \frac{-3}{4\pi}\sqrt{\frac{1}{2}}\langle EQ_1 \sin\theta\cos\theta e^{-i\phi}\rangle_{\mathbf{r}} = 0.$$

Taking into account that the elements of matrix EQ_ℓ present a dependence on the polar angle θ in the function of $\sin^2\theta$, one obtains integral expression $\int_0^\pi EQ_\ell \cos\theta\sin\theta d\theta = 0$. Therefore, the following two matrix blocks in matrix (45) are zero:

$$B_{13} = \frac{\sqrt{3}}{4\pi}\langle EQ_1\cos\theta\rangle_{\mathbf{r}} = 0,$$
$$B_{31} = \frac{\sqrt{3}}{4\pi}\langle EQ_0\cos\theta\rangle_{\mathbf{r}} = 0.$$

The double integrals involved in each matrix block in the characteristic Eq. (46) can be calculated with respect to the variable ϕ, reducing them into simple integrations with respect to θ. For example, the calculation of matrix block B_{11} can be performed as the following:

$$\begin{aligned}B_{11} &= \frac{1}{4\pi}\langle EQ_0\rangle_{\mathbf{r}} \\ &= \frac{\epsilon}{2}\begin{pmatrix} \chi_0^+\left\langle\frac{1}{\lambda-\eta}\right\rangle_{\mathbf{r}} & -\chi_0^-\left\langle\frac{z_0^2}{\lambda-\eta}\right\rangle_{\mathbf{r}} \\ -\chi_0^+\left\langle\frac{z_0^{*2}}{\lambda-\eta^*}\right\rangle_{\mathbf{r}} & \chi_0^-\left\langle\frac{1}{\lambda-\eta^*}\right\rangle_{\mathbf{r}} \end{pmatrix} \\ &= \frac{\epsilon}{4}\begin{pmatrix} \chi_0^+\int_0^\pi \frac{\sin\theta}{\lambda-\eta}d\theta & 0 \\ 0 & \chi_0^-\int_0^\pi\frac{\sin\theta}{\lambda-\eta^*}d\theta \end{pmatrix} \\ &= \frac{\epsilon}{4}\begin{pmatrix} \chi_0^+\int_{-1}^1\frac{dx}{\lambda-\eta} & 0 \\ 0 & \chi_0^-\int_{-1}^1\frac{dx}{\lambda-\eta^*} \end{pmatrix}.\end{aligned}$$

All other components B_{jk} can be calculated similarly, which yields

$$\begin{aligned}B_{22} &= \frac{3}{8\pi}\langle EQ_1\sin^2\theta\rangle_{\mathbf{r}} \\ &= \frac{\epsilon}{8}\begin{pmatrix} \chi_1^+\int_{-1}^1\frac{1-x^2}{\lambda-\eta}dx & 0 \\ 0 & \chi_1^-\int_{-1}^1\frac{1-x^2}{\lambda-\eta^*}dx \end{pmatrix},\end{aligned}$$

$$\begin{aligned}B_{24} &= -\frac{3}{8\pi}\langle EQ_1\sin^2\theta e^{2i\phi}\rangle_{\mathbf{r}} \\ &= -\frac{\epsilon}{8}\begin{pmatrix} 0 & 0 \\ \chi_1^+\int_{-1}^1\frac{(1-x^2)h^{*2}R^2}{\lambda-\eta^*}dx & 0 \end{pmatrix},\end{aligned}$$

$$\begin{aligned}B_{33} &= \frac{3}{4\pi}\langle EQ_1\cos^2\theta\rangle_{\mathbf{r}} \\ &= \frac{\epsilon}{4}\begin{pmatrix} \chi_1^+\int_{-1}^1\frac{x^2dx}{\lambda-\eta} & 0 \\ 0 & \chi_1^-\int_{-1}^1\frac{x^2dx}{\lambda-\eta^*} \end{pmatrix},\end{aligned}$$

$$\begin{aligned}B_{42} &= -\frac{3}{8\pi}\langle EQ_1\sin^2\theta e^{-2i\phi}\rangle_{\mathbf{r}} \\ &= -\frac{\epsilon}{8}\begin{pmatrix} 0 & \chi_1^-\int_{-1}^1\frac{(1-x^2)h^2R^2}{\lambda-\eta}dx \\ 0 & 0 \end{pmatrix},\end{aligned}$$

and

$$B_{44} = B_{22}.$$

Here, the functions $R = R(x)$, $\eta = \eta(x)$, and $h = h(x)$ are to be taken as the following:

$$R(x) = a_1\sqrt{1 - x^2},$$

$$\eta(x) = i\sqrt{\Delta^2 - a_1^2(1 - x^2)},$$

$$h(x) = \frac{1}{\Delta + \sqrt{\Delta^2 - a_1^2(1 - x^2)}}.$$

We note that the functions $\chi_\ell^\pm$ for $\ell = 0, 1$ are given by

$$\chi_0^\pm(\lambda) = \tfrac{1}{2}\big[1 + e^{-(\lambda \pm i\Omega)\tau}\big],$$

$$\chi_1^\pm(\lambda) = \tfrac{3}{4}\big[1 - e^{-(\lambda \pm i\Omega)\tau}\big].$$

[1] A. Pikovsky, M. Rosenblum, and J. Kurths, *Synchronization: A Universal Concept in Nonlinear Sciences* (Cambridge University Press, Cambridge, UK, 2001).

[2] S. H. Strogatz, *Sync: The Emerging Science of Spontaneous Order* (Hyperion, New York, 2003).

[3] Y. Kuramoto, *Chemical Oscillations, Waves, and Turbulence* (Springer, New York, 1984).

[4] J. A. Acebron, L. L. Bonilla, C. J. Perez Vicente, F. Ritort, and R. Spigler, The Kuramoto model: A simple paradigm for synchronization phenomena, Rev. Mod. Phys. **77**, 137 (2005).

[5] S. H. Strogatz, From Kuramoto to Crawford: Exploring the onset of synchronization in populations of coupled oscillators, Physica D **143**, 1 (2000).

[6] *Spirals and Vortices*, edited by K. Tsuji and S. C. Müller (Springer, Cham, 2019).

[7] A. V. Panfilov, Spiral breakup as a model of ventricular fibrillation, Chaos **8**, 57 (1998).

[8] J. M. Davidenko, A. V. Pertsov, R. Salomonsz, W. Baxter, and J. Jalife, Stationary and drifting spiral waves of excitation in isolated cardiac muscle, Nature (London) **355**, 349 (1992).

[9] A. T. Winfree, Electrical turbulence in three-dimensional heart muscle, Science **266**, 1003 (1994).

[10] E. M. Cherry, F. H. Fenton, Visualization of spiral and scroll waves in simulated and experimental cardiac tissue, New J. Phys. **10**, 125016 (2008).

[11] X. Huang, W. C. Troy, Q. Yang, H. Ma, C. R. Laing, S. J. Schiff, J.-Y. Wu, Spiral waves in disinhibited mammalian neocortex, J. Neuroscience **24**, 9897 (2004).

[12] Y. Kuramoto and D. Battogtokh, Coexistence of coherence and incoherence in nonlocally coupled phase oscillators, Nonlinear Phenom. Complex Syst. **5**, 380 (2002).

[13] D. M. Abrams and S. H. Strogatz, Chimera states for coupled oscillators, Phys. Rev. Lett. **93**, 174102 (2004).

[14] A. E. Motter, Spontaneous synchrony breaking, Nat. Phys. **6**, 164 (2010).

[15] M. J. Panaggio and D. M. Abrams, Chimera states: Coexistence of coherence and incoherence in networks of coupled oscillators, Nonlinearity **28**, R67 (2015).

[16] E. Schöll, Synchronization patterns and chimera states in complex networks: Interplay of topology and dynamics, Eur. Phys. J. Spec. Top. **225**, 891 (2016).

[17] O. E. Omel'chenko, The mathematics behind chimera states, Nonlinearity **31**, R121 (2018).

[18] S. Majhi, B. K. Bera, D. Ghosh, M. Perc, Chimera states in neuronal networks: A review, Phys. Life Rev. **28**, 100 (2019).

[19] F. Parastesh, S. Jafari, H. Azarnoush, Z. Shahriari, Z. Wang, S. Boccaletti, and M. Perc, Chimeras, Phys. Rep. **898**, 1 (2021).

[20] Y. Kuramoto and S. Shima, Rotating spirals without phase singularity in reaction-diffusion systems, Prog. Theor. Phys. Suppl. **150**, 115 (2003).

[21] S. Shima and Y. Kuramoto, Rotating spiral waves with phase-randomized core in nonlocally coupled oscillators, Phys. Rev. E **69**, 036213 (2004).

[22] J. Davidsen, Symmetry-breaking spirals, Nat. Phys. **14**, 207 (2018).

[23] C. Laing, The dynamics of chimera states in heterogeneous Kuramoto networks, Physica D **238**, 1569 (2009).

[24] C. Gu, G. St-Yves, and J. Davidsen, Spiral wave chimeras in complex oscillatory and chaotic systems, Phys. Rev. Lett. **111**, 134101 (2013).

[25] E. A. Martens, C. Laing, and S. H. Strogatz, Solvable model of spiral wave chimeras, Phys. Rev. Lett. **104**, 044101 (2010).

[26] O. E. Omel'chenko, M. Wolfrum, S. Yanchuk, Y. L. Maistrenko, and O. Sudakov, Stationary patterns of coherence and incoherence in two-dimensional arrays of non-locally coupled phase oscillators, Phys. Rev. E **85**, 036210 (2012).

[27] J. Xie, E. Knobloch, and H.-C. Kao, Twisted chimera states and multicore spiral chimera states on a two-dimensional torus, Phys. Rev. E **92**, 042921 (2015).

[28] O. E. Omel'chenko, M. Wolfrum, and E. Knobloch, Stability of spiral chimera states on a torus, SIAM J. Appl. Dyn. Syst. **17**, 97 (2018).

[29] M. Bataille-Gonzalez, M. G. Clerc, and O. Omel'chenko, Moving spiral wave chimeras, Phys. Rev. E **104**, L022203 (2021).

[30] C. Laing, Chimeras in two-dimensional domains: Heterogeneity and the continuum limit, SIAM J. Appl. Dyn. Syst. **16**, 974 (2017).

[31] M. J. Panaggio and D. H. Abrams, Chimera states on the surface of a sphere, Phys. Rev. E **91**, 022909 (2015).

[32] R.-S. Kim and C.-U. Choe, Symmetry-broken states on a spherical surface of coupled oscillators: From modulated coherence to spot and spiral chimeras, Phys. Rev. E **98**, 042207 (2018).

[33] R.-S. Kim and C.-U. Choe, Chimera state on a spherical surface of nonlocally coupled oscillators with heterogeneous phase lags, Chaos **29**, 023101 (2019).

[34] C.-U. Choe, R.-S. Kim, and H. Jo, Spiral wave chimeras induced by heterogeneity in phase lags and time delays, Physica D **422**, 132892 (2021).

[35] R.-S. Kim, G.-H. Tae, and C.-U. Choe, Emergence of stripe-core mixed spiral chimera on a spherical surface of nonlocally

coupled oscillators, Int. J. Bifurcation Chaos **31**, 2150182 (2021).

[36] C.-U. Choe, M.-S. Ho, and R.-S. Kim, Asymmetric spiral chimeras on a spheric surface of nonlocally coupled phase oscillators, Phys. Rev. E **107**, 024212 (2023).

[37] J. F. Totz, J. Rode, M. R. Tinsley, K. Showalter, and H. Engel, Spiral wave chimera states in large populations of coupled chemical oscillators, Nat. Phys. **14**, 282 (2018).

[38] J. F. Totz, M. R. Tinsley, H. Engel, and K. Showalter, Transition from spiral wave chimeras to phase cluster states, Sci. Rep. **10**, 7821 (2020).

[39] Wai Shing Lee, Edward Ott, and Thomas M. Antonsen, Large coupled oscillator systems with heterogeneous interaction delays, Phys. Rev. Lett. **103**, 044101 (2009).

[40] N. A. Venkov, S. Coombes, P. C. Matthews, Dynamic instabilities in scalar neural field equations with space-dependent delays, Physica D **232**, 1 (2007).

[41] Q. Song, Z. Wang, Neural networks with discrete and distributed time-varying delays: A general stability analysis, Chaos, Solitons Fractals **37**, 1538 (2008).

[42] S. Coombes, Large-scale neural dynamics: Simple and complex, NeuroImage **52**, 731 (2010).

[43] S. Visser, R. Nicks, O. Faugeras, S. Coombes, Standing and travelling waves in a spherical brain model: The Nunez model revisited, Physica D **349**, 27 (2017).

[44] E. Ott and T. M. Antonsen, Low dimensional behavior of large systems of globally coupled oscillators, Chaos **18**, 037113 (2008).

[45] E. Ott and T. M. Antonsen, Long time evolution of phase oscillator systems, Chaos **19**, 023117 (2009).

[46] See Supplemental Material at http://link.aps.org/supplemental/10.1103/PhysRevE.108.054204 for MATLAB code to generate uniformly the points on unit sphere.

[47] V. K. Vanag and I. R. Epstein, Inwardly rotating spiral waves in a reaction-diffusion system, Science **294**, 835 (2001).

[48] E. M. Nicola, L. Brusch, and M. Bär, Antispiral waves as sources in oscillatory reaction-diffusion media, J. Phys. Chem. B **108**, 14733 (2004).

[49] D. V. Ramana Reddy, A. Sen, and G. L. Johnston, Time delay induced death in coupled limit cycle oscillators, Phys. Rev. Lett. **80**, 5109 (1998).

[50] K. Pyragas, Continuous control of chaos by self-controlling feedback, Phys. Lett. A **170**, 421 (1992).

[51] K. Pyragas, Delayed feedback control of chaos, Philos. Trans. R. Soc. A **364**, 2309 (2006).

[52] C.-U. Choe, H. Jang, V. Flunkert, T. Dahms, Philipp Hövel, and E. Schöll, Stabilization of periodic orbits near a subcritical Hopf bifurcation in delay-coupled networks, Dynam. Syst. **28**, 15 (2013).